AIAA JOURNAL
Vol. 40, No. 4, April 2002

Structural and Aeroelastic Modeling of General Planform Wings with Morphing Airfoils

Frank H. Gern,* Daniel J. Inman,† and Rakesh K. Kapania‡
Virginia Polytechnic Institute and State University, Blacksburg, Virginia 24061-0261

By use of equivalent plate modeling, an efficient method has been developed to study the structural behavior and static aeroelastic response of general builtup wing structures composed of skins, spars, and ribs. The model includes transverse shear effects by treating the wing as a plate, following the first-order shear deformation theory. The equations of motion are derived using the Ritz method with Legendre polynomials as trial functions. To model arbitrary wing planforms, the wing is composed of two plates, connected by distributed translatory and rotary springs of very high stiffness. The structural model has been validated for a set of examples by comparing the results with the ones obtained from MSC/NASTRAN. A distributed actuation scheme allows the modification of wing twist and camber for maneuver control of the vehicle. The model has been applied to study the roll performance of a flapless smart wing with morphing airfoils. It has been shown that a wing without conventional, hinged control surfaces can exhibit improved roll performance and an increased roll reversal speed due to both aerodynamic and structural advantages.

Introduction

THE latest generation of uninhabited combat air vehicles (UCAV) currently under investigation may feature a special wing planform with a significant break in the wing's trailing edge, the so-called lambda wing (Fig. 1). The geometry of the lambda wing together with an increased flexibility of the wing structure requires special models for appropriate structural and aeroelastic analyses. Simplified models for aeroelastic investigations with beam or single platelike structural representations are not accurate enough for such low aspect ratio wings with complex planforms. To overcome these drawbacks, a structural model based on an equivalent plate representation has been developed. To account properly for both a complex wing planform and the interior wing structure, the model consists of two wing sections (inboard and outboard section) built up of skins, spars, and ribs. The suitability of equivalent plate models for the structural analysis of aircraft wings has already been described by several authors.[1–3]

In contrast to finite element models, equivalent continuum models are often used to simulate complex structures for the purpose of obtaining global solutions in the early design stages. This idea is reasonable as long as the complex structure physically behaves in a manner similar to the continuum model used and if only global quantities of the response are of concern. A considerable body of literature exists on the static or dynamic behavior of plates. A survey article on this subject listing more than 300 references has been published by Lovejoy and Kapania,[4] covering all sorts of thin, thick, laminated or composite plates of trapezoidal shapes. The employed first-order shear deformation theory (FSDT) is based on the Reissner–Mindlin model. In this model, the constraint that a normal to the midsurface remains normal to the midsurface after deformation is relaxed, and a uniform transverse shear strain is allowed. Because of its simplicity and its low requirements regarding computational capacity, this FSDT is the most widely used theory for thick and anisotropic laminated plates.

The Rayleigh–Ritz method is applied to solve the resulting equivalent plate problem, with the Legendre polynomials being used as the trial functions. After the stiffness and mass matrices are determined by applying the Lagrange equations, structural analysis can be readily performed. Natural frequencies and mode shapes of the wing can be obtained by solving an eigenvalue problem. Static deformations due to concentrated forces or aerodynamic loads are obtained by solving a linear system of equations. The problem is formulated in such a way that no limitation is placed on the wing thickness distribution. To validate the present method, a generic lambda wing featuring skins, spars, and ribs is analyzed. The results are compared with the ones obtained from a detailed finite element analysis using MSC/NASTRAN.

Structural Modeling

A detailed description of the representation of the different structural wing elements (skins, spars, and ribs) used with the present model may be found in Ref. 3. To model the special planform of a lambda wing, two trapezoidal plates have to be joined. As outlined in the Appendix, this is achieved by application of linear and rotational springs with very large magnitudes of stiffness on the plate boundaries at the wing break. In such a way, it is also possible to approximate the boundary conditions of clamped edges. Similarly, applying only linear springs of very large stiffness on the plate boundaries approximates the boundary conditions for simply supported edges. Details of these practices may be found in Refs. 4 and 5.

Aerodynamic Modeling

To find the static aeroelastic response of the lambda wing, the aerodynamic loads are calculated based on the vortex lattice method (VLM). For this purpose, a linearized compressible VLM code has been employed. A detailed description of the aerodynamic load calculation may be found in Ref. 6. To account for compressibility effects, the airflow density is corrected according to the freestream Mach number using the internal Prandtl–Glauert correction. Although not capable of transonic shock predictions, this modification allows an acceptable prediction of the wing's pressure distribution and local lift coefficients.

To account for the spanwise variation of the sectional pitch and dihedral, as well as the chordwise variation of the airfoil camber surface, the flow tangency boundary condition is formulated as

$$U_\infty \sin(\alpha - \delta)\cos\gamma = w_{ab}\cos\gamma\cos\delta + v_{ab}\sin\gamma\cos\delta - u_{ab}\cos\gamma\sin\delta \tag{1}$$

Received 17 October 2000; accepted for publication 17 September 2001.

*Research Assistant Professor, Department of Mechanical Engineering Center for Intelligent Material Systems and Structures; currently Manager, New Business Development, Avionics Specialties, Inc., Charlottesville, VA 22906-6400. Member AIAA.

†George R. Goodson Professor and Director, Department of Mechanical Engineering Center for Intelligent Material Systems and Structures. Associate Fellow AIAA.

‡Professor, Department of Aerospace and Ocean Engineering. Associate Fellow AIAA.

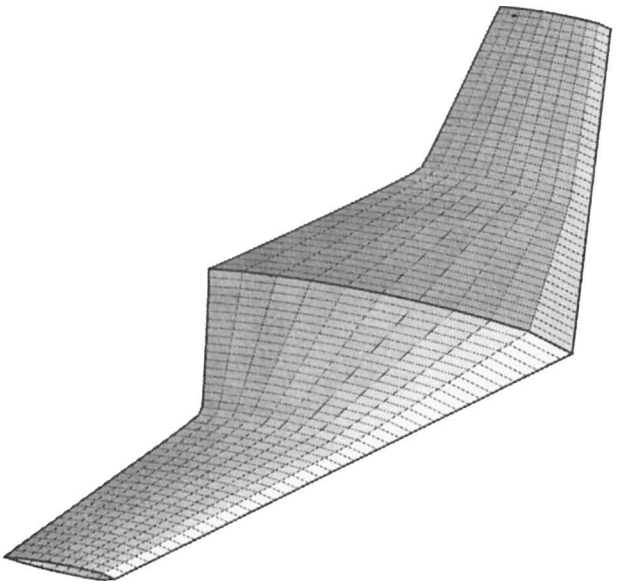

Fig. 1 Generic UCAV with lambda wing.

In Eq. (1), α, δ, and γ are the angle of attack, slope of the mean camber line, and dihedral, respectively, for each point on the curved surface. The induced velocities u_{ab}, v_{ab}, and w_{ab} are the backwash, sidewash, and downwash velocities, respectively, acting on any arbitrary point $C\,(x_c, y_c, z_c)$ of the lifting surface due to a bound vortex AB having the vortex strength Γ and the endpoints $A\,(x_a, y_a, z_a)$ and $B\,(x_b, y_b, z_b)$.

For accurate aerodynamic load prediction, both the inboard and outboard wing section have been subdivided into a lattice of 10 chordwise × 10 spanwise equally spaced vortex panels, yielding a total of 200 vortex panels. The control point of the bound vortex has been fixed at the three-quarter chord position of each panel.

Validation

To validate the structural model, a generic lambda wing structure with the structural and geometric properties as given in Tables 1 and 2 has been analyzed. The wing is being clamped at the wing root. To check the integrity of the present method, results obtained via the equivalent plate modeling technique have been compared to the results obtained from a finite element simulation.

The finite element calculations are made using MSC/NASTRAN, employing 238 nodes and 848 elements. The wing skins are modeled as shell elements (CQUAD4), the spar and rib caps are represented as bar elements (CBAR), and the spar and rib webs are modeled using shear panel elements (CSHEAR).

Mode Shapes and Natural Frequencies

The natural frequencies and mode shapes of the wing can be found by solving the eigenvalue problem

$$[K - \lambda M]\{x\} = 0 \tag{2}$$

where $\lambda = \omega^2$ is an eigenvalue of the system of equations, ω is the corresponding frequency in radians per second, and $\{x\}$ is the respective eigenvector. $[K]$ and $[M]$ are the stiffness and mass matrices calculated as outlined in the Appendix.

Figure 2 compares the mode shapes and natural frequencies of the five lowest vibrational modes of the wing obtained from the present model with the ones obtained from the finite element simulation. It can be seen that both mode shapes and natural frequencies are well predicted by the present method as compared to the finite element method. The relative differences between the natural frequencies obtained from the two different methods for the depicted modes are within less than 3.8%. Note that the results of the equivalent plate analysis have been obtained using a model of 250 degrees of freedom, as compared to the finite element analysis with a model of 1428 degrees of freedom.

Table 1 Generic lambda wing planform geometric data

Parameter	Value
Halfspan	4.57 m (15.0 ft)
Spanwise wing break location	2.02 m (6.63 ft, 44% span)
Chord length at centerline	5.53 m (18.14 ft)
Chord length at break	2.55 m (8.37 ft)
Chord length at tip	1.7 m (5.58 ft)
Thickness/chord ratio at centerline	10.0%
Thickness/chord ratio at break	8.0%
Thickness/chord ratio at tip	8.0%
Leading-edge sweep angle	35 deg

Table 2 Generic lambda wing structural data

Parameter	Value
Number of spars (inboard section)	6
Number of spars (outboard section)	6
Number of ribs (inboard section)	8
Number of ribs (outboard section)	8
Skin thickness	1.5 mm (0.059 in.)
Height of spar caps	2.5 mm (0.0985 in.)
Width of spar caps	3.16 mm (0.1243 in.)
Thickness of spar webs	1.5 mm (0.059 in.)
Height of rib caps	2.5 mm (0.0985 in.)
Width of rib caps	3.16 mm (0.1243 in.)
Thickness of rib webs	1.5 mm (0.059 in.)
Young's modulus	70.0 GPa (1.015×10^7 psi)
Mass density	2700 kg/m^3 (2.526×10^{-4} lb · s^2/in.^{4})
Poisson ratio	0.3

For this specific wing configuration, the vibration characteristics are dominated by the outboard part of the wing, which features relatively thin airfoil sections (Table 1). On the other hand, the thickness of the inboard wing section is relatively high because it is also merging into the fuselage of the UCAV.

Static Deformation

To check further the accuracy of the present method, the deformation of the wing due to a static load has been calculated. For this purpose, the wing tip has been subjected to an upward pointing load of 10,000 lb. The deformation of the wing structure may then be obtained by solving the system

$$[K]\{q\} = \{P\} \tag{3}$$

with $\{P\}$ the generalized load vector applied to the wing structure.

Figure 3 compares the deformation of the wing obtained for the 10,000-lb (44,482-N) tip load applied at 50% of the tip chord with the result obtained from the finite element simulation. Both methods predict the maximum displacement to appear at the trailing edge of the wing. The relative deviation of the results for the maximum displacement is 4.3% [13.9 in. (0.353 m) for the present method as compared to 13.3 in. (0.338 m) for the finite element simulation].

Static Aeroelastic Response

The selected lambda wing planform has been optimized for minimum induced drag at cruise conditions. This has been achieved using Lamar's wing design program LAMDES.[7] For a given wing planform, LAMDES computes the wing twist and airfoil camber distribution required to obtain an elliptical spanload, that is, to minimize the induced drag. The optimization has been performed for high-altitude cruise with a reference dynamic pressure of 150 lb/ft^2 (1.04 psi) at a cruise Mach number of 0.85. A relatively low design lift coefficient of 0.3 was selected for the UCAV wing. In such a way, sufficient additional lift can be generated at lower altitudes, thus ensuring the possibility of both high load factors and superior maneuverability. This is of special concern for the investigated UCAV-type vehicle, where load factors of up to 25 g are anticipated.[8] The aircraft pitch (incidence) was set to zero for the considered flying wing configuration, which yielded an almost symmetrical flight envelope for positive and negative load factors. The mean camber lines at different span stations obtained from LAMDES for both inboard and outboard wing sections are shown in Fig. 4.

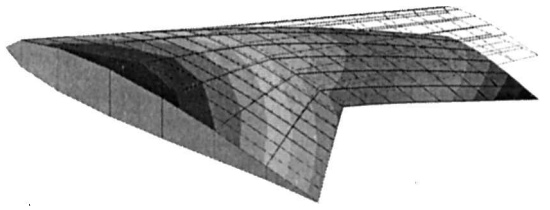

Equivalent plate modeling, mode 1 (f = 15.46 Hz)

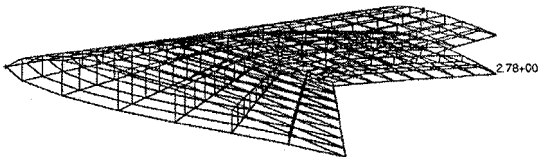

NASTRAN, mode 1 (f = 16.07 Hz)

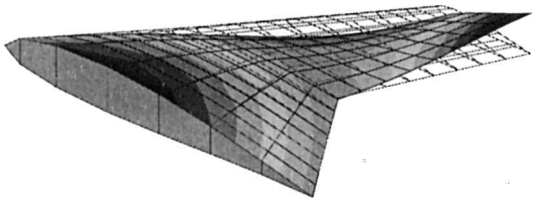

Equivalent plate modeling, mode 2 (f = 52.70 Hz)

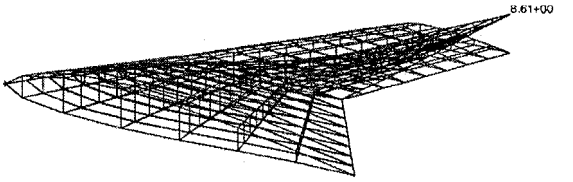

NASTRAN, mode 2 (f = 54.66 Hz)

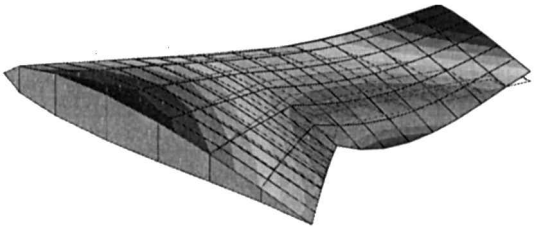

Equivalent plate modeling, mode 3 (f = 64.06 Hz)

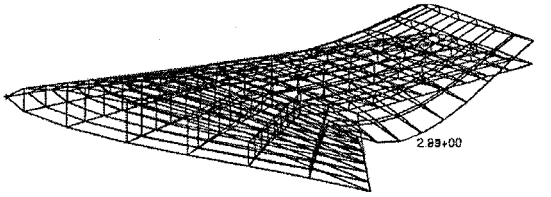

NASTRAN, mode 3 (f = 65.09 Hz)

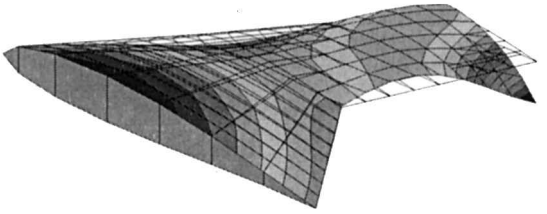

Equivalent plate modeling, mode 4 (f = 109.79 Hz)

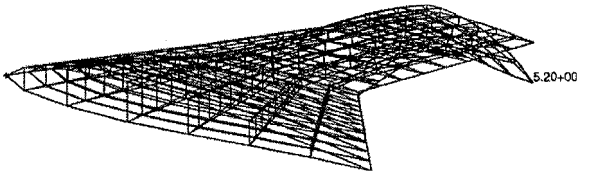

NASTRAN, mode 4 (f = 110.27 Hz)

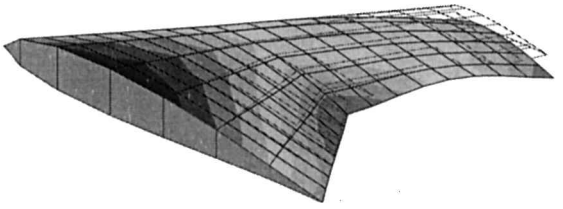

Equivalent plate modeling, mode 5 (f = 118.44 Hz)

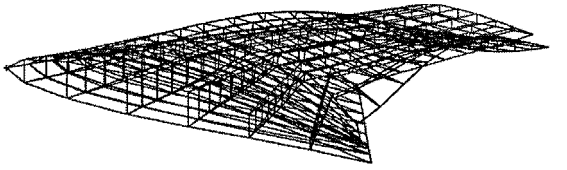

NASTRAN, mode 5 (f = 118.64 Hz)

Fig. 2 Comparison of mode shapes and natural frequencies for a generic lambda wing.

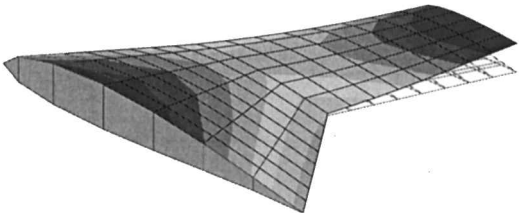

Equivalent plate modeling: wing tip deflection at trailing edge: 13.9 in. (0.353 m)

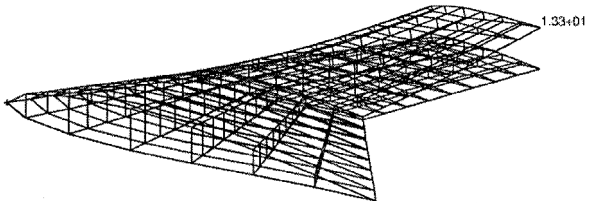

NASTRAN: wing tip deflection at trailing edge: 13.3 in. (0.338 m)

Fig. 3 Wing tip deflection of a generic lambda wing due to an upward pointing 10,000-lb load applied at the wing tip.

The aeroelastic analysis of this configuration has been performed for a dynamic pressure of 782.8 lb/ft^2 (5.436 psi) (3.75×10^4 Pa), corresponding to a Mach number of 0.728 and a dive speed of 553 mph (247 m/s) at sea level.[9] Under these conditions, aeroelastic deformations of the flexible wing lead to a redistribution of the wing spanload, resulting in a slightly different total lift coefficient of the wing. Therefore, by using an iterative procedure, the pitch angle of the vehicle has been adjusted to 0.41 deg to maintain a constant total lift coefficient of 0.3.

For the aeroelastic analysis in NASTRAN, the lambda wing has been modeled as two interfering lifting surfaces. Both inboard and outboard wing sections have been subdivided into 10 chordwise and 10 spanwise aerodynamic panels, yielding a total number of 200 aerodynamic boxes for one-half of the vehicle and providing an aerodynamic modeling similar to the one applied with the equivalent plate analysis. The aerodynamic loads are calculated using the doublet lattice method for the flight conditions given earlier. The camber/twist distribution obtained from LAMDES has been accommodated in NASTRAN using the direct matrix input feature, which allows for a manual modification of the aerodynamic influence coefficient matrix.[10] To create identical conditions for both analyses, the pitch angle of the vehicle has been preset in NASTRAN to the

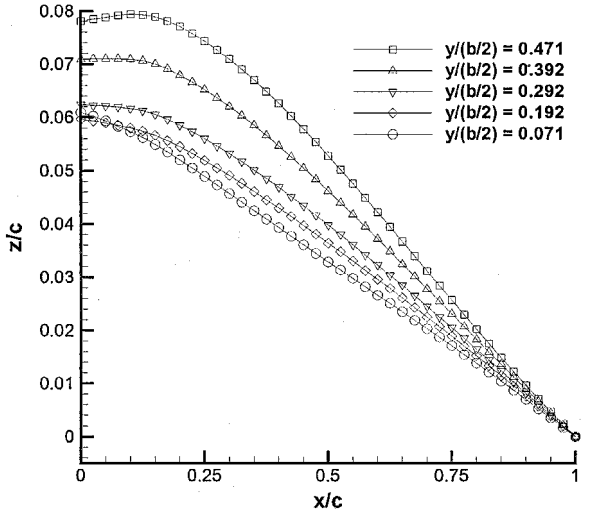

Inboard wing section

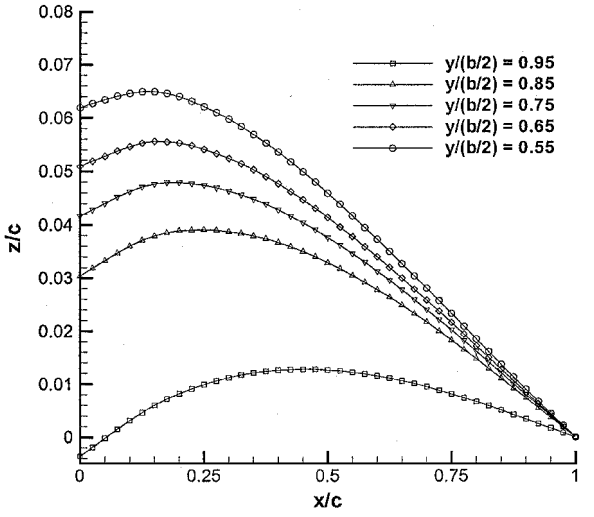

Outboard wing section

Fig. 4 Mean camber lines of the investigated lambda wing at different nondimensional spanwise locations $y/(b/2)$ obtained LAMDES.[7]

value obtained from the iterative procedure in the equivalent plate analysis (0.41 deg).

Figure 5 shows the aeroelastic deformation of the lambda wing for a dynamic pressure of 782.8 lb/ft^2 (5.436 psi) (3.75×10^4 Pa), corresponding to a Mach number of 0.728 and a dive speed of 553 mph (247 m/s) at sea level, obtained from both of the analyses, equivalent plate modeling and NASTRAN. For both models, the maximum tip displacement of the wing structure due to the aerodynamic loads is predicted at the trailing edge. With a displacement of 7.09 in. (0.18 m) for the present model compared to 7.03 in. (0.179 m) for the NASTRAN analysis, the relative deviation of the results is less than 1%. Further comparisons of the wing tip displacements at the leading edge and of the induced twist are given in Table 3. The induced twist at the wing tip has been calculated from the wing tip displacements and the predictions from both aeroelastic models agree well. Compared to NASTRAN, the induced wing twist is slightly overpredicted by the equivalent plate model. These differences can be explained by the simplifying assumptions introduced with the shear modeling as outlined in the Appendix. A detailed assessment of the influence of shear modeling for equivalent plate representations is given in Ref. 2 and would, therefore, be beyond the scope of this paper.

Figure 6 compares the spanwise distribution of the induced wing twist obtained from both models. Note that despite that an FSDT has been used for structural modeling, the calculated induced wing twist appears to have a horizontal tangent at the wing root. This behavior would be consistent with a structural model perfectly rigid in shear, that is, Kirchhoff's assumption.[11] In the present case, the

Table 3 Comparison of selected results of the static aeroelastic analysis for the generic lambda wing obtained via equivalent plate modeling and NASTRAN

Parameter	Equivalent plate model	NASTRAN
Aircraft pitch angle (incidence), deg	0.41[a]	0.41[b]
Wing tip displacement (leading edge), in. (m)	5.8596 (0.149)	5.9275 (0.150)
Wing tip displacement (trailing edge), in. (m)	7.0865 (0.180)	7.0262 (0.179)
Induced twist at wing tip, deg	−1.05	−0.94
Total wing lift coefficient	0.3[c]	0.31

[a]Obtained from an iterative procedure to maintain a constant total wing lift coefficient of 0.3.
[b]Preset to the value obtained from the equivalent plate analysis.
[c]Wing design lift coefficient.

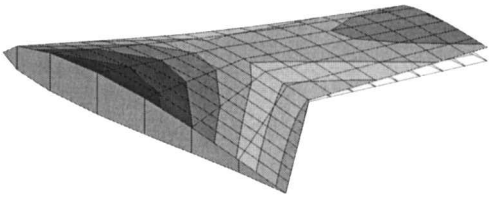

Equivalent plate modeling: wing tip deflection at trailing edge: 7.09 in. (0.18 m)

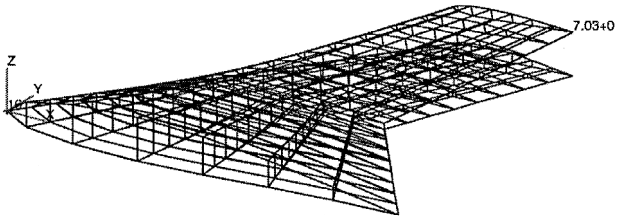

NASTRAN: wing tip deflection at trailing edge: 7.03 in. (0.179 m)

Fig. 5 Aeroelastic deformation of the generic lambda wing with pitch angle of the vehicle adjusted to 0.41 deg to maintain a constant lift coefficient of 0.3.

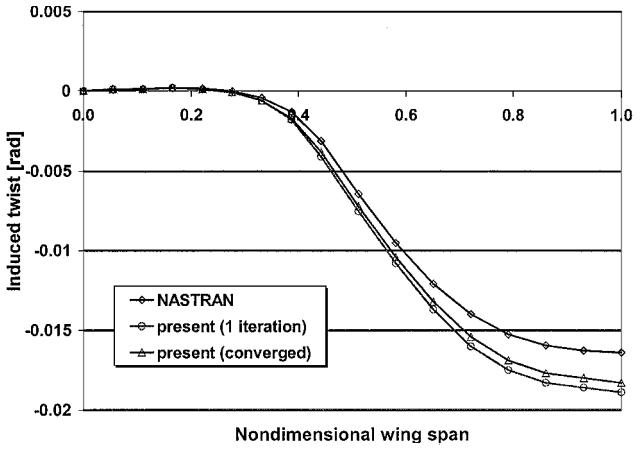

Fig. 6 Comparison of induced wing twist calculated for generic lambda wing using equivalent plate modeling and NASTRAN.

observed elastic wing twist behavior is purely due to the special geometry of the investigated lambda wing planform. The inboard wing/fuselage of the UCAV shows a swept-back leading edge but a highly forward-swept trailing edge. As a result, a fictitious elastic axis of this wing section would exhibit a negative sweep angle. Therefore, due to the aerodynamic bending/twist coupling, the inboard wing section shows the typical behavior of a forward-swept wing, that is, an increase in the induced twist due to aeroelastic deformations (wash-in). The observed forward-swept wing behavior is relatively weak due to the comparably high stiffness of the inboard wing section/fuselage. In the same sense, a fictitious elastic axis of the outboard wing section would be swept back, exhibiting

the typical passive load alleviation behavior of swept-back wings due to aeroelastic deformations (wash-out). The combination of both effects leads to the unconventional double-curved spanwise induced twist distribution as shown in Fig. 6. (Note that in this paragraph the expression fictitious elastic axis is used. The reason for the employment of plate models for structural and aeroelastic analyses of unconventional, low aspect ratio wing planforms is exactly the inaccuracy of beam models together with the assumption of an elastic axis. However, imagining the existence of an elastic axis is very helpful to explain the complex aeroelastic behavior of this wing.)

To check the integrity of the aerodynamic load prediction, the spanload distribution obtained from the present model has been compared to the one obtained from the aerostatic recovery data in the NASTRAN output. Figure 7 shows the calculated spanloads for both a rigid and a flexible wing structure. In the present model, the spanload of the rigid wing is obtained when the aerodynamics are initially computed based on the given wing planform data and camber/twist distribution. The spanload of the deformed wing is calculated in an iterative procedure, by computing the wing deformation due the aerodynamic loads and subsequent updating of the downwash distribution for the VLM according to the wing deformation. In NASTRAN, the spanload of the rigid wing may be obtained by increasing the elastic modulus of the material by a factor of 1000. As can be seen in Fig. 7, the results from the present model agree well with the ones computed by NASTRAN for both the rigid and the flexible wing structure.

As a final check of the aeroelastic model, the total lift coefficient of the flexible UCAV wing has been calculated from the NASTRAN output. Summing up the aerodynamic lift forces computed for the individual aerodynamic boxes in NASTRAN gives the total lift of the wing. Accordingly, the total lift coefficient of the wing can be simply calculated as

$$c_L = L/q\,S_{\text{ref}} \tag{4}$$

where L is the total lift of the wing, q is the dynamic pressure, and S_{ref} is the reference area of the wing planform. When this method is used for the NASTRAN data, the calculated total lift coefficient of the wing is equal to 0.31, that is, the relative difference of the results between both models is 3.3%.

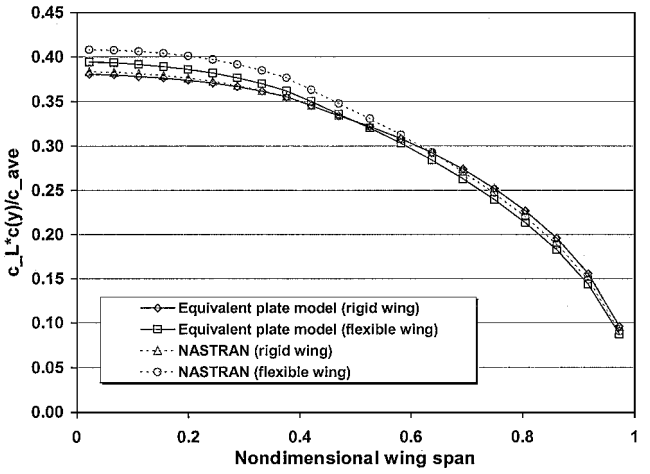

Fig. 7 Comparison of calculated spanload for generic lambda wing using equivalent plate modeling and NASTRAN for flexible and rigid wing structure.

Distributed Structural Actuation

A distributed structural actuation scheme has been implemented to obtain any desired twist or camber deformation of the wing structure. For the investigated vehicle configuration, the inboard wing section/fuselage is relatively rigid. Therefore, only the outboard section of the wing will be fully actuated (Fig. 8). Distributed actuation of the outboard wing can be achieved by placing actuators at the spanwise rib stations. More radical concepts may even completely remove the ribs or foresee adaptive ribs for morphing the airfoil. To analyze the deformation behavior of this structural actuation scheme using the equivalent plate model, the individual actuator forces are replaced by the equivalent moments they create within the wing structure (Fig. 9).

Note that the objective of the present study is to build a structural and aeroelastic model suitable to investigate different actuation concepts. This model will then be used to compute necessary actuator forces, moments, strokes, and power requirements to satisfy given vehicle performance requirements. Because of this generic approach, no attempt has been made so far to optimize the actuator distribution or structural wing configuration to minimize actuation energy and required actuator power (structural flexibility

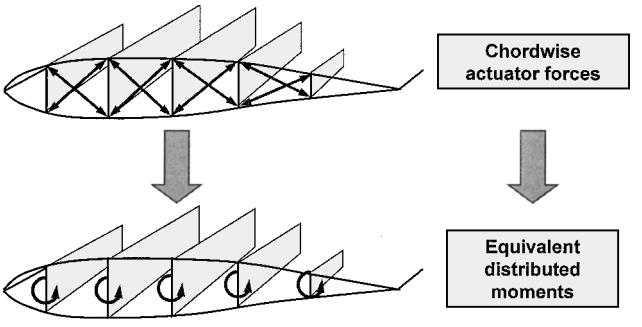

Fig. 9 Actuator forces as distributed moments for the equivalent plate modeling.

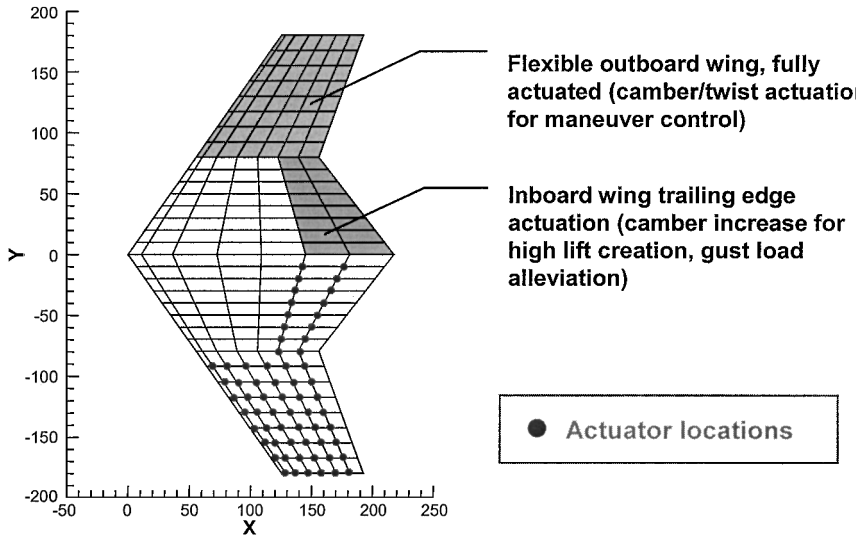

Fig. 8 Distributed actuation of the outboard wing for the investigated vehicle.

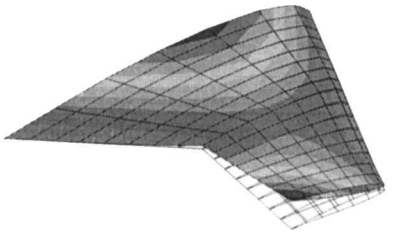

Equivalent plate modeling, twist actuation, trailing edge up [maximum deflection 15.9 in. (0.404 m)]

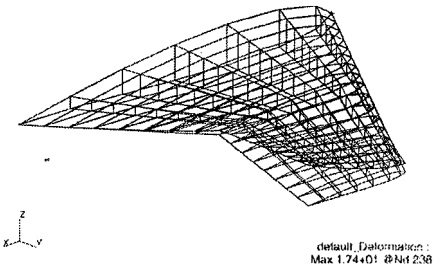

NASTRAN, twist actuation, trailing edge up [maximum deflection 17.4 in. (0.442 m)]

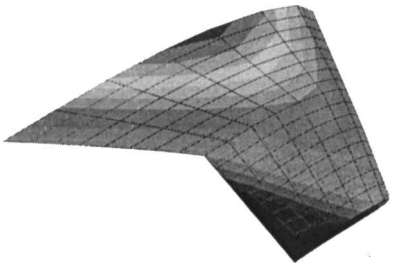

Equivalent plate modeling, twist actuation, trailing edge down [maximum deflection −15.9 in. (−0.404 m)]

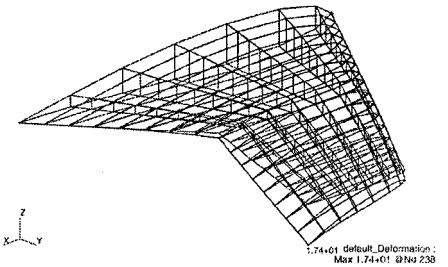

NASTRAN, twist actuation, trailing edge down [maximum deflection −17.4 in. (−0.442 m)]

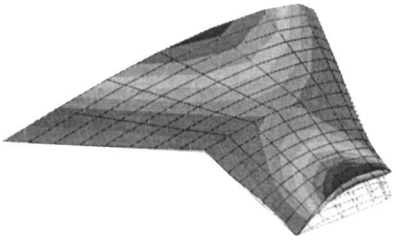

Equivalent plate modeling, camber actuation, positive [maximum deflection 1.56 in. (3.96 cm)]

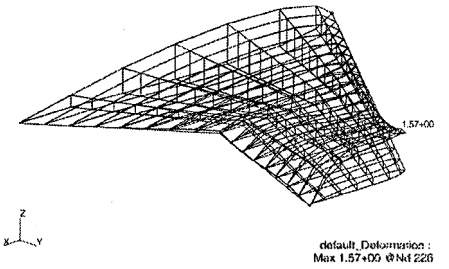

NASTRAN, camber actuation, positive [maximum deflection 1.57 in. (3.99 cm)]

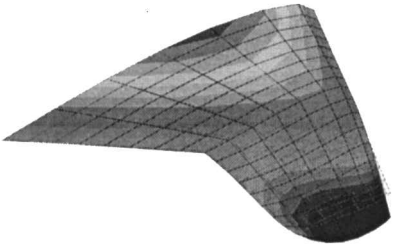

Equivalent plate modeling, camber actuation, negative [maximum deflection −1.56 in. (−3.96 cm)]

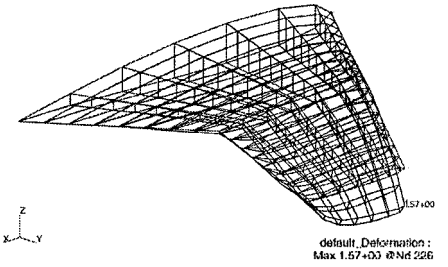

NASTRAN, camber actuation, negative [maximum deflection −1.57 in. (−3.99 cm)]

Fig. 10 Comparison of twist and camber deformation for generic lambda wing obtained using distributed structural actuation of the outboard wing.

tailoring). The actual realization of such a distributed structural actuation scheme will require further assessment in the future. Ongoing work employs the model presented herein for this purpose.

Activation of the actuators in a way that all of the resulting moments are of the same sign, that is, producing a torque in the same direction, will enable one to twist the wing in either direction, trailing edge up or down. If the resulting moments near the leading and trailing edge of the wing are of opposite signs, the camber shape of the airfoil can be modified. Therefore, based on the input from the flight control system, any combination of twist and camber actuation of the wing can be realized. It is anticipated that these modifications of twist and camber, that is, morphing airfoils, can be used for maneuver control of the vehicle.

Figure 10 shows twist and camber deformations resulting from the described distributed wing actuation obtained from equivalent plate modeling and NASTRAN. To outline the basic effects, the actuator force has been kept constant at all actuator locations, varying only the signs of the moments to produce twist or camber actuation. To induce significant wing deformations for illustrative purposes, a relatively high actuator force of 10,000 lb (44,482 N) has been assumed, creating a twist rotation of 13 deg at the wing tip. Much smaller deformations and actuator forces are expected for maneuver control of the vehicle. As can be seen from Fig. 10, wing deformations obtained from NASTRAN agree within 8% (twist actuation) and 1% (camber actuation) with the ones obtained from the equivalent plate model.

Investigation of Roll Performance

Baseline Model

The validated aeroelastic model has been used to study the roll reversal of smart wings with morphing airfoils. To establish a baseline for performance comparisons, a lambda wing featuring a conventional trailing-edge flap has been investigated first. For this purpose, the earlier described structural and aerodynamic models have been extended to capture the deflection of a trailing-edge flap. This can be achieved by additional modifications of the aerodynamic influence

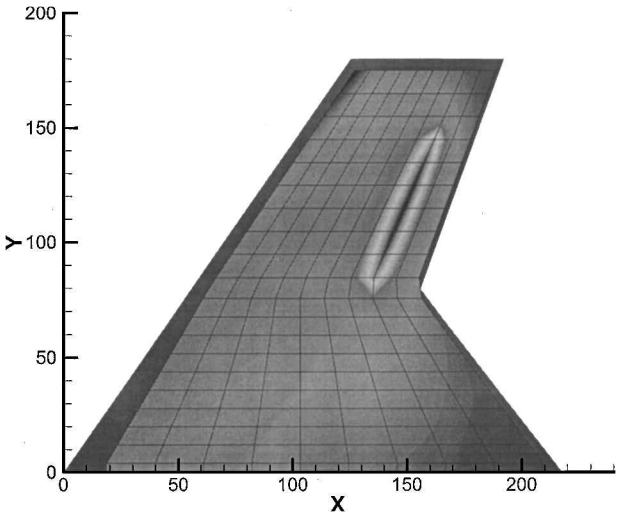

Fig. 11 Nondimensional pressure distribution on the investigated wing planform for a 15-deg downward deflected trailing-edge flap.

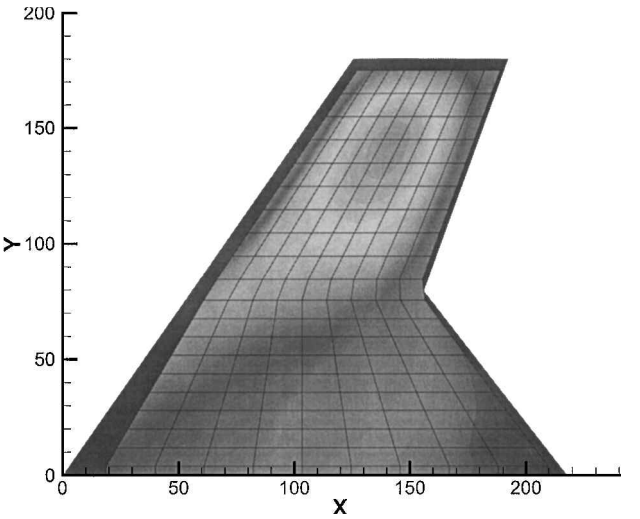

Fig. 12 Nondimensional pressure distribution on the investigated wing planform for a smart wing with morphing airfoils; camber increase of outboard wing section is equivalent to a 15-deg downward deflected trailing-edge flap.

coefficient matrix, introducing the lift and camber increase due to the deflected flap as an additional downwash on the respective aerodynamic panels. Necessary structural modifications are the recalculation of the wing stiffness matrix to account for the actual dimensions of the structural wing box chord. Depending on the actual configuration, the length of the structural wing box chord is between 50 and 70% of the length of the airfoil chord due to flaps and slats attached to the leading and trailing edges of the wing. For the investigated planform, the wing box is assumed to be 70% of the actual airfoil chord.

Figure 11 shows the calculated pressure distribution on the investigated UCAV wing for a 15-deg downward deflected trailing-edge flap. The significant suction peak at the leading edge of the flap is typical due to the sharp change in the downwash distribution of the lifting surface and has been well described in the literature (e.g., Ref. 12). During high-angle-of-attack maneuvers and high load factors, this peak very often is a source of flow separation, leading to a loss of flap effectiveness. Recalculation of the total wing lift coefficient for the wing with deflected flap assuming aerodynamic symmetry yields a value of 0.47 or a c_L increase of 0.17 (57%). The Fig. 11 grid is the aerodynamic control point grid, with the control points located at the three-quarter chord of each aerodynamic panel.

Smart Wing with Morphing Airfoils

The investigated smart wing is a wing without any hinged control surfaces. Instead, the forces and moments required for maneuver control of the vehicle will be provided by modifications to the airfoil geometry of the wing, that is, morphing airfoils. In the present example, the earlier described c_L increase due to a flap deflection is achieved by an increase of the airfoil camber of the morphing wing. Initial investigations are focusing on possible improvements with regard to aerodynamic and aeroelastic characteristics of the vehicle. To benefit from the high flexibility of the outboard wing section and to increase the leverage of the rolling moment, only the outboard wing of the UCAV is actuated as already described. The airfoil camber of the outboard wing is increasing linearly from the wing break to the wing tip. The camber increase is calibrated to yield the same c_L increase as the 15-deg downward deflected flap, that is, an increase from 0.3 to 0.47.

Figure 12 shows the pressure distribution obtained for the earlier described actuation model of the smart wing. As can be seen from Fig. 12, omitting hinged control surfaces is promising for improvements in the aerodynamic quality of the wing. The pressure distribution of the smart wing does not show the significant suction peak of a hinged flap. Furthermore, the absence of sharp edges and vertical or deflected surfaces significantly reduces the radar signature and visibility of the vehicle, thus enhancing its stealth properties. The Fig. 12 grid is the aerodynamic control point grid, with the control points located at the three-quarter chord of each aerodynamic panel.

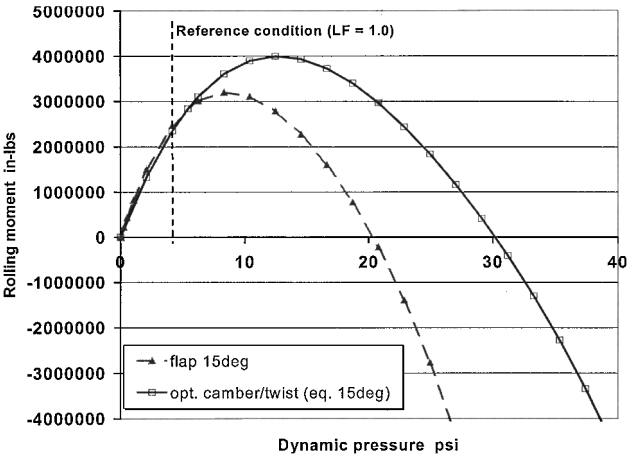

Fig. 13 Rolling moment vs dynamic pressure for the lambda wing with trailing-edge flap compared to morphing airfoils.

Roll Performance and Roll Reversal

Roll performance as a measure of smart wing effectiveness has been investigated by several authors[13–15] and is, therefore, used for the performance evaluation of the wing with morphing airfoils. Figure 13 shows the rolling moment of the investigated lambda wing vs dynamic pressure for both types: wing with trailing edge flap and wing with morphing airfoils. For the comparison, flap deflection and wing morphing have been calibrated to yield identical rolling moments at the reference condition: 782.8-lb/ft^2 [5.436-psi (3.75×10^4 Pa)] dynamic pressure, corresponding to a Mach number of 0.728 or a dive speed of 553 mph (247 m/s) at sea level.[9] In Fig. 13, flap deflection (15 deg) and wing morphing (equivalent to 15 deg at reference conditions) have been kept constant, and only the dynamic pressure has been varied.

For dynamic pressures lower than the reference pressure, both wings exhibit similar rolling moments. For higher dynamic pressures, the morphing wing is able to produce much higher rolling moments than its conventional counterpart. Roll reversal of the morphing wing occurs at dynamic pressures of about 50% higher than for the conventional wing. Two main reasons may be identified for this increase in roll performance of the morphing wing:

1) In contrast to the conventional wing with a trailing-edge flap, the morphing wing does not show the significant suction peak at the hinge line of the flap (compare Figs. 11 and 12). Therefore, the resulting aerodynamic moment of the wing tends to compensate partly for the induced wing twist due to the aeroelastic deformation of the lifting surface and to attenuate the wash-out effect. In contrast,

the suction peak created by the deflected flap shifts the lift resultant toward the trailing edge of the wing, thus increasing the induced wing twist and promoting wash-out.

2) Because of the control surface hinge lines, wing box sections close to the leading and trailing edges of the wing provide little to no structural stiffness. Because there are no hinge lines on a wing with morphing airfoils, consideration of the entire airfoil section yields a higher stiffness of the wing structure. As a result of this increased wing stiffness, aeroelastic deformations are reduced, thus increasing roll performance and roll reversal speed.

Conclusions

A method for structural and aeroelastic analysis of arbitrary planform wings composed of skins, spars, and ribs has been developed. Comparison of the obtained results with finite element calculations in NASTRAN for different test cases has shown the accuracy of the method for design purposes. Based on the assumption that the wing structure behaves like a plate whose deformation can be modeled by the FSDT, the Rayleigh–Ritz method is applied to solve the plate problem with the Legendre polynomials as trial functions. After validation, the model has been used to study the roll performance of smart UCAV wings featuring morphing airfoils. For this purpose, a generic distributed actuation scheme has been implemented and validated via NASTRAN finite element analyses.

It has been shown that a wing without conventional, hinged control surfaces can exhibit improved roll performance and an increased roll reversal speed due to both aerodynamic and structural advantages. Such an increase in roll performance and reversal speed would allow 1) the realization of more lightweight and more flexible wing structures for a given vehicle performance or flight envelope or 2) an expanded flight envelope due to higher roll performance and higher roll reversal speeds. Ongoing work in this project is based on the presented structural and aeroelastic smart wing model to optimize actuator locations and control laws, to minimize actuation power, and to determine forces, moments, strokes, and time constants required for smart wing actuators to employ smart wings with morphing airfoils for primary flight control.

Appendix: Structural Modeling

A detailed description of the representation of the different structural wing elements (skins, spars, and ribs) used with the present model may be found in Refs. 3 and 16. The structural model is based on the FSDT. Note that FSDT introduces the inconsistency of a nonzero shear stress at the top and bottom surfaces of the plate and ignores the variation of the shear strain across the plate thickness. According to the FSDT, the displacement field assumes that 1) a line normal to the nondeformed middle surface remains straight after deformation and 2) the transverse normal stress can be neglected in the constitutive relations.

As a result, the linear displacement field of a single plate is given as

$$u(x, y, z, t) = u_0(x, y, t) + z\phi_x(x, y, t) \tag{A1a}$$

$$v(x, y, z, t) = v_0(x, y, t) + z\phi_y(x, y, t) \tag{A1b}$$

$$w(x, y, z, t) = w_0(x, y, t) \tag{A1c}$$

where u, v, and w are displacements in the x, y, and z directions respectively, subscript 0 refers to quantities associated with the plane $z = 0$, and ϕ_x and ϕ_y are the rotations about the y and $-x$ axis, respectively. It is assumed that the middle surface of the plate is either without or with a very small curvature; therefore $z = 0$ can be considered to be the middle surface.

As long as the wing is of a small thickness-to-chord ratio, the assumption of the wing behaving like a plate is reasonable. For the convenience of calculation, a transformation from the (x, y) to a new (ξ, η) coordinate system is performed. As a result, the wing configuration in the (x, y) plane, a skewed trapezoidal, is being transformed to a square in the (ξ, η) plane.[3]

The displacement components in the plane $z = 0$ in Eqs. (A1), that is, u_0, v_0, w_0, ϕ_x, and ϕ_y, are then expressed as

$$\{u_0, v_0, w_0, \phi_x, \phi_y\}^T = [H]\{q\} \tag{A2}$$

where

$$\{q\} = \left\{\{q_U\}^T, \{q_V\}^T, \{q_W\}^T, \{q_X\}^T, \{q_Y\}^T\right\}^T \tag{A3}$$

is the generalized displacement vector with

$$\{q_U\} = \{U_{11}, U_{12}, \ldots, U_{1J}, U_{21}, \ldots, U_{2J}, \ldots, U_{I1}, \ldots, U_{IJ}\}^T \tag{A4a}$$

$$\{q_V\} = \{V_{11}, \ldots, V_{KL}\}^T \tag{A4b}$$

$$\{q_W\} = \{W_{11}, \ldots, W_{MN}\}^T \tag{A4c}$$

$$\{q_X\} = \{X_{11}, \ldots, X_{PQ}\}^T \tag{A4d}$$

$$\{q_Y\} = \{Y_{11}, \ldots, Y_{RS}\}^T \tag{A4e}$$

The matrix $[H]$ is given by

$$[H] = \text{diag}\left[\{B_{IJ}\}^T, \{B_{KL}\}^T, \{B_{MN}\}^T, \{B_{PQ}\}^T, \{B_{RS}\}^T\right] \tag{A5}$$

where

$$\{B_{\mu\nu}\} = \{B_1(\xi)B_1(\eta), B_1(\xi)B_2(\eta), \ldots, B_\mu(\xi)B_\nu(\eta)\}^T$$

$$\mu\nu = IJ, KL, MN, PQ, RS \tag{A6}$$

is the Ritz base function vector, in which $B_i(x)$ are chosen as Legendre polynomials.

Stiffness Matrix of a Single Plate

The strain energy of a wing structure is given as

$$U = \frac{1}{2}\iiint_V \{\varepsilon\}^T[D]\{\varepsilon\}\,\mathrm{d}V \tag{A7}$$

Note that it is assumed that $\{\sigma\} = [D]\{\varepsilon\}$ and $[D]^T = [D]$. The integration domain V in Eq. (A7) includes all and only the spaces occupied by the components of the wing. After some operations, Eq. (A7) can be rewritten as

$$U = \frac{1}{2}\iiint_V \{q\}^T[C]^T[T]^T[D][T][C]\{q\}\,\mathrm{d}V \tag{A8}$$

After expressing the strain energy of the wing structure as

$$U = \tfrac{1}{2}\{q\}^T[K]\{q\} \tag{A9}$$

comparison of Eqs. (A8) and (A9) gives

$$[K] = \iiint_V [C]^T[T]^T[D][T][C]\,\mathrm{d}V \tag{A10}$$

which is the stiffness matrix of the wing in terms of the generalized displacement vector $\{q\}$. The constitutive matrix $[D]$ is different for the different parts of the wing structure.

Mass Matrix of a Single Plate

The kinetic energy of a wing structure is

$$T = \frac{1}{2}\iiint_V \rho\bar{v}^2\,\mathrm{d}V = \frac{1}{2}\iiint_V \rho\{\bar{v}\}^T\{\bar{v}\}\,\mathrm{d}V \tag{A11}$$

where $\{\bar{v}\}$ is the velocity vector. $[H]$ is defined in Eq. (A5), and $\{\dot{q}\}$ is the time derivative of $\{q\}$ yielding

$$T = \frac{1}{2}\iiint_V \rho\{\dot{q}\}^T[H]^T[ZZ][H]\{\dot{q}\}\,\mathrm{d}V \tag{A12}$$

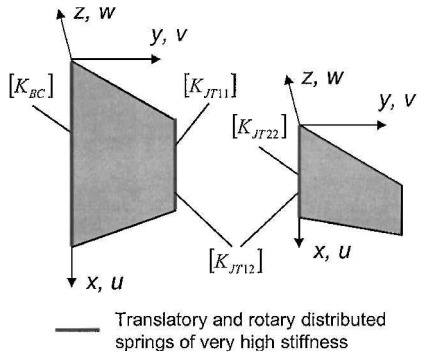

Fig. A1 Joining of two plates for equivalent plate modeling of arbitrary planform wings.

After a similar procedure, comparing the kinetic energy

$$T = \tfrac{1}{2}\{\dot{q}\}^T[M]\{\dot{q}\} \tag{A13}$$

with Eq. (A12), we find that

$$[M] = \iiint_V \rho[H]^T[ZZ][H]\,\mathrm{d}V \tag{A14}$$

which is the mass matrix of the wing in terms of the general velocity vector $\{\dot{q}\}$.

Joining the Plates

To model the special planform of a lambda wing, two trapezoidal plates built up as described earlier have to be joined. This can be achieved by the application of linear and rotational springs with very large magnitudes of stiffness on the plate boundaries at the wing break (Fig. A1). In such a way, it is also possible to approximate the boundary conditions of clamped edges. Similarly, applying only linear springs of very large stiffness on the plate boundaries approximates the boundary conditions for simply supported edges. Details of these practices may be found in Ref. 4.

Stiffness Matrix of the Complete Wing

After joining two plates, the total strain energy of the wing structure is given by

$$U = \tfrac{1}{2}\{q_1\}^T[K_1]\{q_1\} + \tfrac{1}{2}\{q_2\}^T[K_2]\{q_2\} + U_{JT} + \tfrac{1}{2}\{q_1\}^T[K_{BC}]\{q_1\} \tag{A15}$$

where $[K_1]$ and $[K_2]$ are the stiffness matrices for the two plates, $[K_{BC}]$ is the stiffness matrix for the large springs simulating the boundary conditions at the root,[1–3] and U_{JT} is the strain energy relating to the joint between the plates.[5]

After a coordinate transformation to rectangular plates as described in Ref. 3, the relationships between the displacement vectors and the general displacement vectors in the (ξ_1, η_1) and (ξ_2, η_2) planes of the two plates can be written as

$$\{u_1\} = [H_1]\{q_1\} \tag{A16a}$$

$$\{u_2\} = [H_2]\{q_2\} \tag{A16b}$$

where $[H_1]$ and $[H_2]$ are functions of (ξ_1, η_1) and (ξ_2, η_2), respectively. For the joint joining the two parts of the wing, we have

$$-1 \le \xi_1 \le 1, \qquad \eta_1 = 1, \qquad -1 \le \xi_2 \le 1, \qquad \eta_2 = -1$$

By expressing the displacement vector for plate 2 (ξ_2, η_2) in terms of plate 1 (ξ_1, η_1), we obtain

$$\{u_2'\} = [R]\{u_2\} \tag{A17}$$

where $\{u_2'\}$ are the displacements of plate 2 expressed in terms of the plate 1 coordinate system (ξ_1, η_1). Now, the strain energy of the joint can be rewritten as

$$U_{JT} = \tfrac{1}{2}\{u_1 - u_2'\}^T[K_{JT}]\{u_1 - u_2'\} \tag{A18}$$

where $[K_{JT}]$ is the stiffness matrix for the joint. Springs of very high stiffness can be used if the joint is rigid. When Eq. (A17) is replaced in Eq. (A18), the strain energy of the joint can be expressed in terms of the displacement vectors of plates 1 and 2:

$$U_{JT} = \tfrac{1}{2}(\{u_1\} - [R]\{u_2\})^T[K_{JT}](\{u_1\} - [R]\{u_2\}) \tag{A19}$$

A generalized displacement vector for the whole system can now be constructed as

$$\{q\} = \begin{Bmatrix}\{q_1\}\\ \{q_2\}\end{Bmatrix} \tag{A20}$$

When Eqs. (A16) are used, the total strain energy of the wing structure can be written in terms of this generalized displacement vector:

$$\begin{aligned} U = \frac{1}{2}\{q\}^T[K]\{q\} &= \frac{1}{2}\begin{Bmatrix}\{q_1\}\\ \{q_2\}\end{Bmatrix}^T\begin{bmatrix}[K_{11}] & [K_{12}]\\ [K_{21}] & [K_{22}]\end{bmatrix}\begin{Bmatrix}\{q_1\}\\ \{q_2\}\end{Bmatrix}\\ &= \frac{1}{2}\{q_1\}^T[K_{11}]\{q_1\} + \frac{1}{2}\{q_1\}^T\left([K_{12}] + [K_{21}]^T\right)\\ &\quad\times\{q_2\} + \frac{1}{2}\{q_2\}^T[K_{22}]\{q_2\} \end{aligned} \tag{A21}$$

When Eq. (A21) is compared with Eqs. (A15) and (A19), the stiffness matrix of the complete wing structure in terms of the generalized displacements $\{q\}$is obtained:

$$[K] = \begin{bmatrix}[K_{11}] & [K_{12}]\\ [K_{21}] & [K_{22}]\end{bmatrix} \tag{A22}$$

In Eq. (A22), the different submatrices are given by

$$[K_{11}] = [K_1] + [H_1]^T[K_{JT}][H_1] + [K_{BC}] \tag{A23a}$$

$$[K_{22}] = [K_2] + [H_2]^T[R]^T[K_{JT}][R][H_2] \tag{A23b}$$

$$[K_{12}] = [K_{21}]^T = -\tfrac{1}{2}[H_1]^T\left([K_{JT}][R]^T + [K_{JT}]^T[R]\right)[H_2] \tag{A23c}$$

Mass Matrix of the Complete Wing

The mass matrix of the complete wing structure is obtained in a similar way to that described earlier for the stiffness matrix. The total kinetic energy of the wing structure is

$$\begin{aligned} T &= \frac{1}{2}\{\dot{q}_1\}^T[M_1]\{\dot{q}_1\} + \frac{1}{2}\{\dot{q}_2\}^T[M_2]\{\dot{q}_2\}\\ &= \frac{1}{2}\begin{Bmatrix}\{\dot{q}_1\}\\ \{\dot{q}_2\}\end{Bmatrix}^T\begin{bmatrix}[M_1] & 0\\ 0 & [M_2]\end{bmatrix}\begin{Bmatrix}\{\dot{q}_1\}\\ \{\dot{q}_2\}\end{Bmatrix} \end{aligned} \tag{A24}$$

where $[M_1]$ and $[M_2]$ are the mass matrices of the inboard and outboard wing sections.[3] Therefore, the mass matrix of the entire structure is

$$[M] = \begin{bmatrix}[M_1] & 0\\ 0 & [M_2]\end{bmatrix} \tag{A25}$$

Acknowledgments

This project is sponsored by the Air Force Office of Scientific Research and the Defence Advanced Research Projects Agency under Grant F49620-99-1-0294, with Brian Sanders and Ephrahim Garcia as Technical Monitors. The authors would also like to thank Terrence Weisshaar, Harobert Robertshaw, Gregory Pettit, and Anand Natarajan for valuable discussions. Special thanks are due to Youhua Liu for providing his computer program for the structural analysis of a single plate wing and to Erwin Sulaeman for his contributions to the vortex lattice code.

References

[1]Giles, G. L., "Equivalent Plate Analysis of Aircraft Wing Box Structures with General Planform Geometry," *Journal of Aircraft*, Vol. 23, No. 11, 1986, pp. 859–865.

[2]Livne, E., and Navarro, I., "Nonlinear Equivalent Plate Modeling of Wing-Box Structures," *Journal of Aircraft*, Vol. 36, No. 5, 1999, pp. 851–864.

[3]Kapania, R. K., and Liu, Y., "Static and Vibration Analyses of General Wing Structures Using Equivalent-Plate Models," *AIAA Journal*, Vol. 38, No. 7, 2000, pp. 1269–1277.

[4]Lovejoy, A. E., and Kapania, R. K., "Natural Frequencies and Atlas of Mode Shapes for Generally-Laminated, Thick, Skew, Trapezoidal Plates," Center for Composite Materials and Structures, Rept. CCMS-94-09, Virginia Polytechnic Inst. and State Univ., Blacksburg, VA, Aug. 1994.

[5]Tizzi, S., "Numerical Procedure for the Dynamic Analysis of Three-Dimensional Aeronautical Structures," *Journal of Aircraft*, Vol. 34, No. 1, 1997, pp. 120–130.

[6]Gern, F. H., Sulaeman, E., Naghshineh-Pour, A., Kapania, R. K., and Haftka, R. T., "Structural Wing Sizing for Multidisciplinary Design Optimization of a Strut-Braced Wing," *Journal of Aircraft*, Vol. 38, No. 1, 2001, pp. 154–163.

[7]Lamar, J. E., "A Vortex Lattice Method for the Mean Camber Shapes of Trimmed Non-Coplanar Planforms with Minimum Vortex Drag," NASA TN D-8090, June 1976.

[8]Anderson, J. D., *Aircraft Performance and Design*, WCB/McGraw–Hill, Boston, 1999, p. 544.

[9]Bisplinghoff, R. L., Ashley, H., and Halfman, R. L., *Aeroelasticity*, Dover, Mineola, NY, 1996, p. 467.

[10]Rodden, W. P., and Johnson, E. H., "MSC/NASTRAN, Aeroelastic Analysis, User's Guide," Ver. 68, MacNeal–Schwendler Corp., 1995, p. 222.

[11]Gern, F. H., and Librescu, L., "Static and Dynamic Aeroelasticity of Advanced Aircraft Wings Carrying External Stores," *AIAA Journal*, Vol. 36, No. 7, 1998, pp. 1121–1129.

[12]Sanders, B., and Eastep, F. E., "Aerodynamic Improvements with Conformal Control Surfaces," *Advances in Computational Engineering and Sciences*, Vol. 2, edited by S. N. Atluri and F. W. Brust, Tech Science Press, Palmdale, CA, 2000, pp. 1550–1555.

[13]Khot, N. S., Appa, K., Ausman, J., and Eastep, F. E., "Deformation of a Flexible Wing Using an Actuating System for a Rolling Maneuver Without Ailerons," AIAA Paper 98-1802, April 1998.

[14]Pendleton, E., Bessette, D., Field, P., Miller, G., and Griffin, K., "The Active Aeroelastic Wing Flight Research Program," AIAA Paper 98-1972, April 1998.

[15]Chen, P. C., Nam, C. H., Sarhaddi, D., Liu, D. D., Griffin, K., Heeg, J., and Yurkovich, R., "Torsion-Free Wing Concept for Enhanced Aircraft Maneuver," AIAA Paper 2000-0223, April 2000.

[16]Liu, Y., Kapania, R. K., Gern, F. H., and Inman, D., "Equivalent Plate Modeling of Arbitrary Planform Wings," *Advances in Computational Engineering and Sciences*, Vol. 1, edited by S. N. Atluri and F. W. Brust, Tech Science Press, Palmdale, CA, 2000, pp. 515–521.

A. Chattopadhyay
Associate Editor